Chemical Science

ROYAL SOCIETY OF CHEMISTRY

EDGE ARTICLE

View Article Online
View Journal | View Issue



Cite this: *Chem. Sci.*, 2025, **16**, 15714

All publication charges for this article have been paid for by the Royal Society of Chemistry

# Synthetic control guided by growth mechanism insights enable tailored precursors for layered oxide cathodes

Hai-Yan Hu,[ab] Yong-Chun Li,*[c] Yan-Fang Zhu,*[ab] Haidong Liu,[ce] Wei Xiang,*[d] Jia-Zhao Wang [b] and Yao Xiao *[ab]

Received 17th June 2025
Accepted 29th July 2025

DOI: 10.1039/d5sc04432d

rsc.li/chemical-science

Comprehending the growth mechanism of precursors is crucial for the industrial fabrication of high-performance $LiNi_{0.8}Co_{0.1}Mn_{0.1}O_2$ (NCM811) cathode materials. Nonetheless, achieving precise control over particle size, morphology, and internal structure remains difficult due to limited understanding of precursor evolution during synthesis. This work tracks real-time reaction parameters and morphological evolution to investigate the growth behavior of $Ni_{0.8}Co_{0.1}Mn_{0.1}(OH)_2$ precursors. Variations in reactant concentration, feed rate, and consumption dynamics affect the observed three-stage growth mechanism of secondary particles. Approximately 2 μm-sized particles are initially generated through nucleation and subsequently aggregate into larger forms. As growth advances, the particle size distribution widens due to continuous nucleation and inhibited aggregation. Primary particles transition from nano-needle to rod-like forms, but their growth becomes increasingly restricted by limited energy and spatial constraints, leading to dense aggregation on pre-existing structures. The intermediate stage emerges as a crucial phase for controlling particle development. Fine-tuning during this stage effectively controls particle coarsening and promotes uniform secondary structures with intricate internal architectures. These observations provide valuable guidance for improving precursor synthesis, allowing for the scalable synthesis of Ni-rich cathode materials with enhanced performance.



## Introduction

Rechargeable lithium-ion batteries (LIBs) are advanced electrochemical energy storage systems widely used in electric vehicles (EVs) and for stationary energy storage applications, offering high energy density, long service life, and stable performance.[1] In comparison with conventional technologies such as lead-acid batteries, LIBs exhibit distinct advantages in energy efficiency, environmental sustainability, and operational longevity.[2–5]

The performance and cost of the battery largely depend on the cathode material.[6–9] For optimal performance, an ideal cathode should show a high redox potential for stable voltage output, preserve structural integrity over repeated charge–discharge cycles, and provide ample lithium-ion intercalation sites.[10–12] Currently commercialized cathode materials include layered oxides (*e.g.*, $LiCoO_2$ and $LiNi_xCo_yMn_{1-x-y}O_2$), spinel oxides (*e.g.*, $LiMn_2O_4$), and olivine-type phosphates (*e.g.*, $LiFePO_4$). Among these, Ni-rich layered oxides have attracted particular interest due to their high capacity, good thermal stability, and excellent cycling performance.[13–18] The development of scalable and controllable synthesis techniques is increasingly critical as the demand for high-performance cathode materials continues to grow.[19–21] To fabricate Ni-rich precursors, several co-precipitation techniques have been investigated.[22] Using carbonate as a chelating agent, the carbonate co-precipitation method gains from the stability of transition metal carbonates ($TMCO_3$), thus enabling the reaction to proceed under air without an inert atmosphere.[23–25] Despite these advantages, it typically yields large secondary particles with low tap density, and $TMCO_3$ decomposes during calcination, releasing $CO_2$, which results in increased porosity and reduced compressibility of the final electrode. Moreover, the significant solubility differences among carbonate salts make it challenging to control the stoichiometry of the final precursor. In contrast, the oxalate co-precipitation method, which employs ammonium oxalate as both the chelating and precipitating agent, allows for the effective co-precipitation of multiple metal ions and facilitates a relatively slow reaction

[a]College of Chemistry and Materials Engineering, Wenzhou University, Wenzhou 325035, P. R. China. E-mail: yanfangzhu@wzu.edu.cn; xiaoyao@wzu.edu.cn
[b]Zhejiang Provincial Key Laboratory of Advanced Battery Materials and Technology, Wenzhou University Technology Innovation Institute for Carbon Neutralization, Wenzhou 325035, P. R. China
[c]Ångström Laboratory, Department of Chemistry, Uppsala University, Uppsala SE 751 21, Sweden. E-mail: yongchun.li@kemi.uu.se
[d]College of Materials and Chemistry and Chemical Engineering, Chengdu University of Technology, Chengdu 610059, P. R. China. E-mail: xiangwei@cdut.edu.cn
[e]Department of Technical Physics, University of Eastern Finland, 70210 Kuopio, Finland

rate. This promotes uniform nucleation and growth of secondary particles, thereby enabling better control over particle morphology.[26] Nevertheless, the method is highly sensitive to synthesis parameters such as pH, temperature, stirring speed, and reaction time. As a result, it presents challenges in process control and typically leads to low tap density of the resultant product. Building upon these approaches, the hydroxide co-precipitation method, which is currently the most widely used in industry, offers significant advantages in terms of process robustness. When combined with high-temperature solid-state reaction, it produces precursors with high tap density, homogeneous morphology, and well-controlled particle size distribution.[27–29] However, to ensure consistent precursor quality, the process involves multiple interdependent variables that require precise regulation. Though much research is being conducted, most studies focus on the kinetics of co-precipitation, providing little insight into the real-time morphological evolution and its impact on important parameters, including tap density and microstructure.[30–32] Understanding the growth mechanism of Ni-rich precursors remains a key challenge, as the size distribution, structural uniformity, and electrochemical performance of the final cathode material are directly influenced by the formation and transformation of primary and secondary particles.

In this work, by tracking real-time reaction parameters and morphological changes, we systematically investigate the growth behavior of $Ni_{0.8}Co_{0.1}Mn_{0.1}(OH)_2$ precursors. The results elucidate a three-stage growth mechanism of secondary particles, driven by alterations in reactant concentration, feed rate, and consumption rate. In the first stage, fine particles of approximately 2 μm are initially generated. These particles aggregate and grow into larger forms in the second stage. Although smaller secondary particles continue to nucleate in the third stage, the overall growth of secondary particles slows, leading to a broader particle size distribution. Primary particles simultaneously change from nano-sized, needle-like forms to elongated rod shapes. Their growth is constrained by limited energy input and spatial confinement, which causes newly formed primary particles to deposit onto existing ones. As secondary particle accumulation progresses, these constraints intensify, resulting in smaller primary particles with denser packing. Importantly, the intermediate stage is identified as a critical window for targeted intervention. Key characteristics for improving the electrochemical performance of the final cathode material are uniformly distributed secondary particles with compact internal architectures, which can be effectively obtained by adjusting process parameters during this stage. Moreover, this control helps to reduce excessive particle coarsening. These findings provide significant new viewpoints on the controlled synthesis of Ni-rich precursors and practical guidance for scalable production of cathode materials with homogeneous particle distribution and optimal tap density.

## Results and discussion

Given that the microscopic structure and electrochemical performance of $LiNi_{0.8}Co_{0.1}Mn_{0.1}O_2$ (NCM811) are strongly influenced by its precursor, precise control over the precursor's morphology and crystal structure is essential for achieving high-quality NCM811.[33] By means of process parameters including pH, ammonia-to-salt ratio, stirring speed, and feed rate, the hydroxide co-precipitation method presents a versatile approach for controlling particle size and morphology, as shown in Fig. 1a and S1 (SI). Two main processes govern particle growth in the hydroxide co-precipitation reaction: (1) in solution, metal ions form complex ions with ammonium that subsequently react with $OH^-$ to generate hydroxide particles; (2) a dynamic equilibrium exists between the metal hydroxide precipitates and the metal complexes, defined by a precipitation–dissolution interaction. This process follows a growth mechanism involving gradual dissolution and recrystallization, as represented by eqn (1) and (2).[34]

$$M^{2+} + nNH_4OH(aq) \rightarrow [M(NH_3)_n]^{2+}(aq) + nH_2O \quad (1)$$

$$[M(NH_3)_n]^{2+}(aq) + 2OH^- \rightarrow M(OH)_2(s)\downarrow + nNH_3 \quad (2)$$

The reaction equations show that the precipitation of transition metal ions during the reaction process is greatly influenced by pH and ammonia concentration.[35] When the pH is too low or the ammonia concentration is elevated, the reduced precipitation rate inhibits nucleation. Conversely, the precipitation rate increases when the pH is too high or the ammonia concentration is low, thus promoting nucleation. Therefore, the synthesis of high-quality precursors depends on controlling both pH and ammonia levels inside the system.[36–38] Apart from pH and ammonia concentration, precursor synthesis is

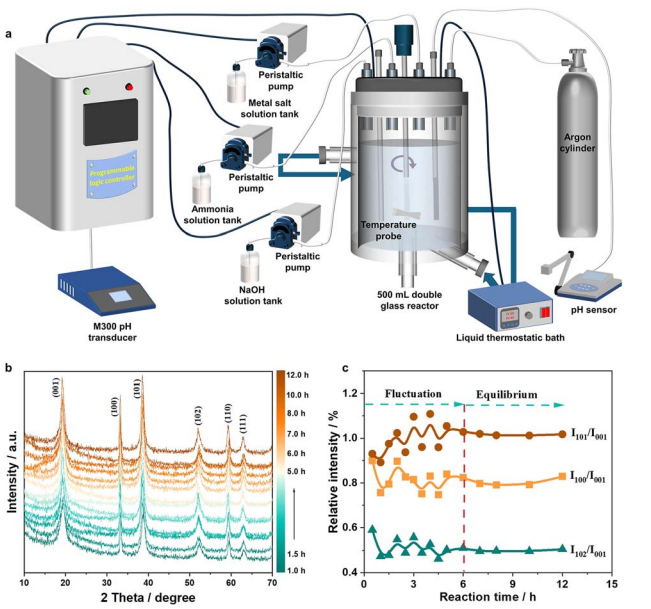


Fig. 1 (a) Schematic diagram illustrating the experimental configuration for precursor synthesis. (b) XRD patterns of $Ni_{0.8}Co_{0.1}Mn_{0.1}(OH)_2$ at various reaction times. (c) The ratios of XRD characteristic peaks (101)/(001), (100)/(001), (102)/(001) for $Ni_{0.8}Co_{0.1}Mn_{0.1}(OH)_2$ at different reaction times.

influenced by feed rate and stirring speed. While a controlled rate guarantees homogeneous particle size, the feed rate influences particle residence time, which in turn affects growth and process efficiency. Stirring speed promotes uniform mixing and efficient mass transfer, ensuring smooth surfaces on secondary particles. Together, these parameters are key to achieving a uniform morphology and high-quality precursor.[39] The optimal co-precipitation conditions are pH 11.1, ammonia-to-salt ratio 1.0, feed rate 1.2 mL $min^{-1}$, and stirring speed 1200 rpm, which yield uniform morphology, good crystallinity, and high tap density based on Fig. S2–S17 (SI). Although extensive research on precursor preparation is underway, direct comparisons of synthesis parameters remain limited due to variations in precursor types, experimental conditions, and operational factors.[40–42] Furthermore, little research has been conducted on the mechanism of precursor growth, which leaves a knowledge gap that impedes comprehension of the complex interactions among synthesis parameters.[43–45] To address this issue, we tracked the evolution of the precursor structure over time. The X-ray diffraction (XRD) patterns of the $Ni_{0.8}Co_{0.1}Mn_{0.1}(OH)_2$ precursor shown in Fig. 1b and S18 (SI) at different reaction times reveal several important aspects. The high purity of the material is verified by the diffraction peaks of the precursor aligning well with β-$Ni(OH)_2$ without any extra impurity peaks.[46,47] Low intensity and broad half-peak widths in the diffraction peaks during the early stages of the reaction point to poor crystallinity of the precursor. As the reaction proceeds, the half-peak widths narrow, and the intensity of the diffraction peaks increases, indicating improved crystallinity in the $Ni_{0.8}Co_{0.1}Mn_{0.1}(OH)_2$ precursor. Especially in the early stages of the reaction, the (101) crystal face exhibits a large exposed area, strong peak intensity, and narrow half-width, reflecting a relatively fast growth rate that is likely driven by its higher surface energy.[48] As the reaction proceeds, the preferential growth gradually shifts from the (101) to the (001) plane, which may result from kinetic factors such as variations in precursor concentration and ion transport dynamics. The evolution of intensity ratios shown in Fig. 1c supports this trend: the $I_{(101)}/I_{(001)}$ ratio increases between 0–6 hours, surpassing 1, then stabilizes around 1 between 6–12 hours. In contrast, the $I_{(100)}/I_{(001)}$ and $I_{(102)}/I_{(001)}$ ratios decrease during the first 6 hours and remain below 1 from 6 to 12 hours. This shift from preferential growth along the (101) plane to more balanced growth between the (101) and (001) planes highlights a critical structural transition, particularly within the first 6 hours, which represents a key window for tuning the crystallographic characteristics of the precursor. A thorough understanding of this crystallization behavior is essential for optimizing precursor synthesis and improving the structure and electrochemical performance of NCM811 materials for energy storage applications.

Further optimization of material properties requires insight into the particle growth evolution and the fundamental processes during synthesis.[49–51] To this end, the evolution of both primary and secondary particles in the $Ni_{0.8}Co_{0.1}Mn_{0.1}(OH)_2$ precursor was examined using scanning electron microscopy (SEM) at various reaction times. Fig. 2a–aa presents the SEM images of the $Ni_{0.8}Co_{0.1}Mn_{0.1}(OH)_2$ precursor at several reaction times, illustrating the evolution of secondary particle morphology. The secondary particles at the 1-hour mark are rather loosely aggregated nanoscale particles with notable agglomeration. As the reaction proceeds to two hours, agglomeration decreases, and the secondary particles gradually develop into micron-sized structures. At 2.5 hours, agglomeration vanishes, and the particles with varying sizes are formed, resulting in a broad size distribution. Subsequently, by 3 hours, smaller secondary particles begin to merge, forming elliptical particles. At 3.5 hours, spherical secondary particles of roughly 2–3 μm appear, and they continue to grow in both quantity and size by 4 hours. By 5 hours, smooth spherical particles with diameters around 5 μm are observed, although the fusion of secondary particles becomes more pronounced. As growth progresses from 6 to 7 hours, the diameter of the secondary particles continues to increase, and the size distribution becomes more uniform. At 8 hours, the secondary particles reach approximately 10 μm, while smaller particles are also present, indicating a gradual disappearance of particle fusion and the onset of new nucleation. Finally, at 12 hours, the precursor evolves into smooth spherical particles with an average diameter of around 12 μm. Notably, from 7 to 12 hours, while the diameter of the secondary particles continues to increase, the presence of smaller particles becomes more prominent, causing a broadening of the particle size distribution (Fig. S19, SI). This phenomenon can be attributed to two main factors: first, as the secondary particles grow larger, new primary particles, limited by energy and space, are unable to continue growing on the existing larger particles, leading to a slower increase in particle diameter. Second, although their consumption decreases with time, the number of primary particles generated remains unchanged due to the steady feeding rate. These unconsumed primary particles subsequently develop into smaller secondary particles, thereby broadening the overall particle size distribution.[52]

High-magnitude SEM images of the primary particles of $Ni_{0.8}Co_{0.1}Mn_{0.1}(OH)_2$ at various reaction times are shown in Fig. 2b–ab. At 1 hour, the primary particles appear as fine needle-like structures with considerable agglomeration and a loose packing arrangement. By 1.5 hours, the primary particles increase in size, but agglomeration remains severe. At 2 hours, there is only a slight change in the size of the primary particles, although their packing becomes denser. As growth progresses to 2.5 hours, the primary particles become significantly elongated. From 3 to 4 hours, some secondary particles fuse together, while the primary particle packing becomes more compact. At 4.5 hours, the primary particles further enlarge and evolve into well-defined elongated nanostructures. In contrast, by 5 hours, a clear reduction in primary particle size is observed, marking the onset of a shrinking trend. The primary particles shrink rapidly between 5 and 7 hours. Subsequently, the decrease in size slows down, while the packing density increases between 8 and 12 hours. This phenomenon can be explained by three factors: first, during the initial stage of the reaction, the newly added raw materials preferentially grow on the existing primary particles. More energy is needed to maintain the

 

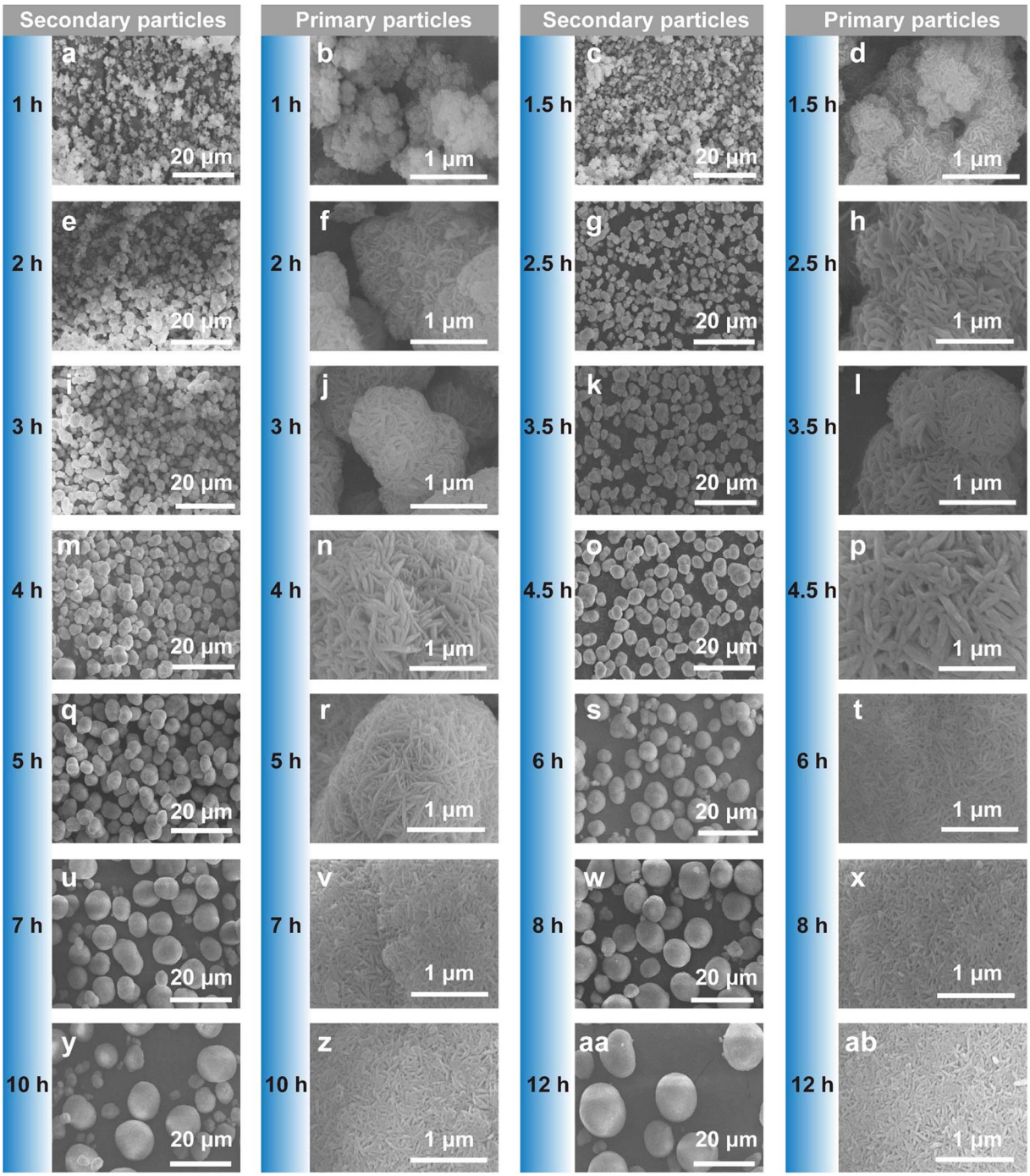


Fig. 2 SEM images of the secondary particles (a–aa) and primary particles (b–ab) for $Ni_{0.8}Co_{0.1}Mn_{0.1}(OH)_2$ at different reaction times.

expansion of these primary particles as they grow larger; however, new primary particles form when the available energy becomes insufficient. Second, the packing of primary particles gets denser as the reaction goes on, so restricting more expansion. Ultimately, as secondary particles grow larger and adopt a more spherical morphology, the increasing surface energy required for continued growth on existing particles leads to the formation of smaller primary particles during the later stages of the reaction. The SEM study provides important new perspectives on the crystallization and growth dynamics of the $Ni_{0.8}Co_{0.1}Mn_{0.1}(OH)_2$ precursor, particularly highlighting the transition from nanoscale agglomerated particles to bigger spherical ones. Notably, the structural evolution observed during the intermediate stage suggests that this period may serve as a key window for controlling primary particle morphology and packing behavior. Such insights are instrumental in optimizing the synthesis process and tailoring the

final material properties for enhanced energy storage performance.

Tailoring the microstructure and packing properties of $Ni_{0.8}Co_{0.1}Mn_{0.1}(OH)_2$ precursors requires an understanding of the temporal evolution of particle size distribution (PSD) and tap density.[53] Fig. 3 systematically demonstrates the evolution of these properties throughout the co-precipitation process. Fig. 3a shows PSD profiles at various synthesis times. All measured distributions approximately follow a normal distribution trend. Interestingly, the frequency distribution is significantly lower during both the early (1–2 h) and late stages (10–12 h) of the reaction, compared to the middle stage (6–8 h), suggesting a narrowing followed by a re-broadening of the PSD throughout the reaction process. In the early stages, a shoulder peak around 1 μm indicates the generation of a high concentration of fine particles resulting from initial nucleation. Later, at the final stage, a secondary peak close to 100 μm appears due to the agglomeration of large secondary particles formed by interparticle fusion. Fig. 3b illustrates the evolution of $D_{50}$ (the median particle diameter) and its corresponding frequency distribution as a function of reaction time. The growth process can be divided into three distinct stages. In Stage I (0–2 h), primary particles of about 2 μm form, and the frequency distribution remains basically unchanged. Together with the SEM results, the low particle concentration in the reactor favors nucleation and slow particle growth, thus producing stable $D_{50}$ and frequency values. In Stage II (2–6 h), both $D_{50}$ and frequency increase steadily, indicating apparent particle coarsening and a narrowing particle size distribution (PSD). This is explained by the secondary particles from existing seeds growing progressively under sufficient precursor supply. In Stage III (6–12 h), $D_{50}$ continues to increase at a slower rate, while the frequency distribution declines sharply. This deceleration in particle growth is likely due to the energy limitations required to support further growth of increasingly large particles. As particle size increases, further surface growth becomes less favorable due to reduced surface curvature, lower supersaturation, and higher interfacial energy barriers. Meanwhile, the feedstock consumption rate decreases, and the excess precursors may no longer be efficiently deposited on existing particles. Instead, these unconsumed reactants can trigger secondary nucleation events, especially under local supersaturation conditions, leading to the formation of finer particles and a broadened size distribution. This re-nucleation broadens the PSD again at the late stage. The variation of tap density as a function of reaction time is shown in Fig. 3c, revealing a non-monotonic trend that aligns with the three growth stages. In Stage I, the tap density increases slowly due to the evolving morphology and loose packing of needle-like primary particles. In Stage II, a more pronounced increase is observed, as secondary particles become larger and more spherical, improving bulk packing efficiency. In Stage III, however, a slight drop in tap density observed at 7–8 h could be the result of the formation of rather large, but rough and poorly flowable secondary particles, generating voids and lowering packing density. Towards the final stage, the generation of numerous small particles helps fill inter-particle voids, thereby increasing tap density. To provide a simplified description of the growth trends, eqn (3) was employed as a schematic approach to represent the relative changes in $D_{50}$, frequency distribution, and tap density, where $M$ denotes each of these parameters, and $t$ corresponds to the reaction time ($h$) (Fig. 3d).

$$\frac{M_{t2} - M_{t1}}{M_{t2}(t2 - t1)} \tag{3}$$

The relative growth curves further illustrate the three-stage behavior described above. In stage I, tap density increases significantly—by more than 30%—driven by structural rearrangements and densification, while the relative growth rates of $D_{50}$ and frequency remain nearly zero. In stage II, $D_{50}$ increases steadily (~15%), the frequency first rises and then drops to zero, and tap density growth begins to plateau. In stage III, $D_{50}$ continues to grow at a lower rate, frequency drops into the negative regime, and tap density fluctuates slightly around zero. In particular, a transient drop in tap density is observed around 7–8 h, corresponding to the morphological evolution evident in SEM. Achieving high volumetric energy density in final cathode materials requires maintaining high tap density and optimizing precursor morphology, and the present results provide valuable guidance toward this goal.[54–56] The electrochemical performance of the obtained material was assessed after sintering in order to confirm the advantages of these ideal conditions. As illustrated in Fig. 3e and f, S20, and Table S1 (SI), the corresponding precursor exhibits the best electrochemical

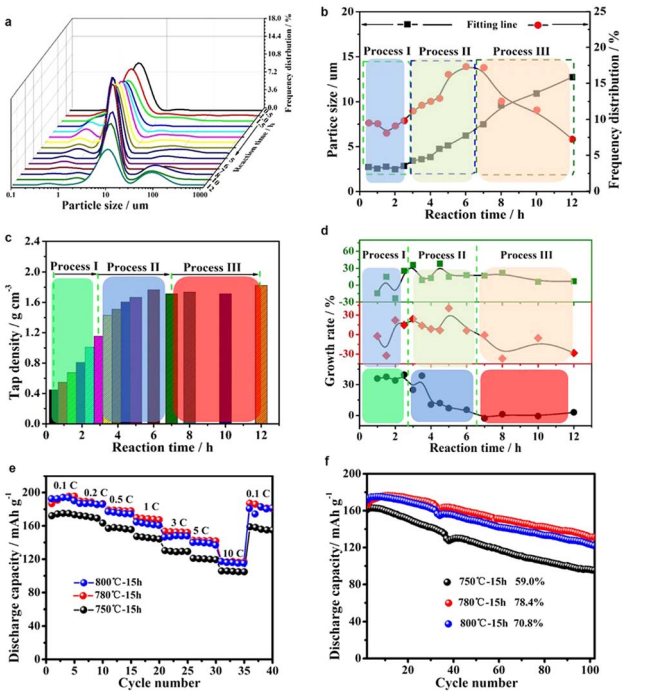


Fig. 3 (a) Particles distribution. (b) $D_{50}$ and frequency distribution. (c) Tap density. (d) Relative growth rate for $Ni_{0.8}Co_{0.1}Mn_{0.1}(OH)_2$ at different reaction time. (e) Rate performance for $LiNi_{0.8}Co_{0.1}Mn_{0.1}O_2$ at different sintering temperatures. (f) Cycling performance at 1 C for $LiNi_{0.8}Co_{0.1}Mn_{0.1}O_2$ at different sintering temperatures.

performance after sintering at 780 °C for 15 h. Specifically, the material delivers a high discharge capacity of up to 198 mA h $g^{-1}$ at 0.1 C (2.7–4.3 V), and an initial reversible capacity exceeding 175 mA h $g^{-1}$ at 1 C, with a capacity retention of 79% after 100 cycles. This performance enhancement is closely related to the co-evolution of PSD, $D_{50}$, frequency distribution, and tap density during co-precipitation, which collectively shape the precursor microstructure and ultimately determine the electrochemical characteristics of the sintered NCM811 cathode.[57–61] These results reinforce the practical value of precisely controlling precursor evolution during the intermediate stage to achieve superior battery performance.

As shown in Fig. 4a and Table S2 (SI), the evolution of secondary particles during precursor synthesis can be divided into three distinct stages. In the first stage, the initially added raw materials rapidly nucleate to form many small primary particles (~1–2 μm). While the particle size remains relatively constant during this period, the number of secondary particles increases and their dispersion improves, suggesting slowed growth. In the second stage, these small particles begin to combine and fuse, which gradually increases the particle size. In the third stage, as the consumption rate of precursors by particle growth becomes lower than the supply rate, new small particles nucleate again. A broadening particle size distribution results from this competitive mechanism between particle growth and nucleation. The primary particles in these secondary agglomerates show a corresponding three-step growth process. Driven by anisotropic energy favoring longitudinal growth, the primary particles in process I initially nucleate and grow from needle-like morphologies into elongated rod-like structures. As the reaction proceeds into process II, increasing energy and spatial constraints progressively limit the growth of these rod-like particles, leading to nucleation of a new generation of finer particles that begin to deposit and grow on the surface of the earlier-formed primary structures. At last, in process III the expansion of both original and newly formed particles becomes progressively restricted, producing smaller, denser particles that pack more tightly within the secondary agglomerates. This progressive densification enhances the compaction and internal microstructural uniformity of the precursor particles, which is critical for achieving high structural integrity in the final material.[62] Further insights into the evolution of particle size and size distribution over time for the conventional and small-particle-controlled routes are provided (Fig. 4b and c). In the conventional route, particle size rises quickly as the reaction proceeds, and the particle size distribution widens as well. Large, non-uniform particle populations thus arise at the end of this process. In contrast, the small-particle-controlled path effectively suppresses excessive particle growth, preserving a smaller average particle size and

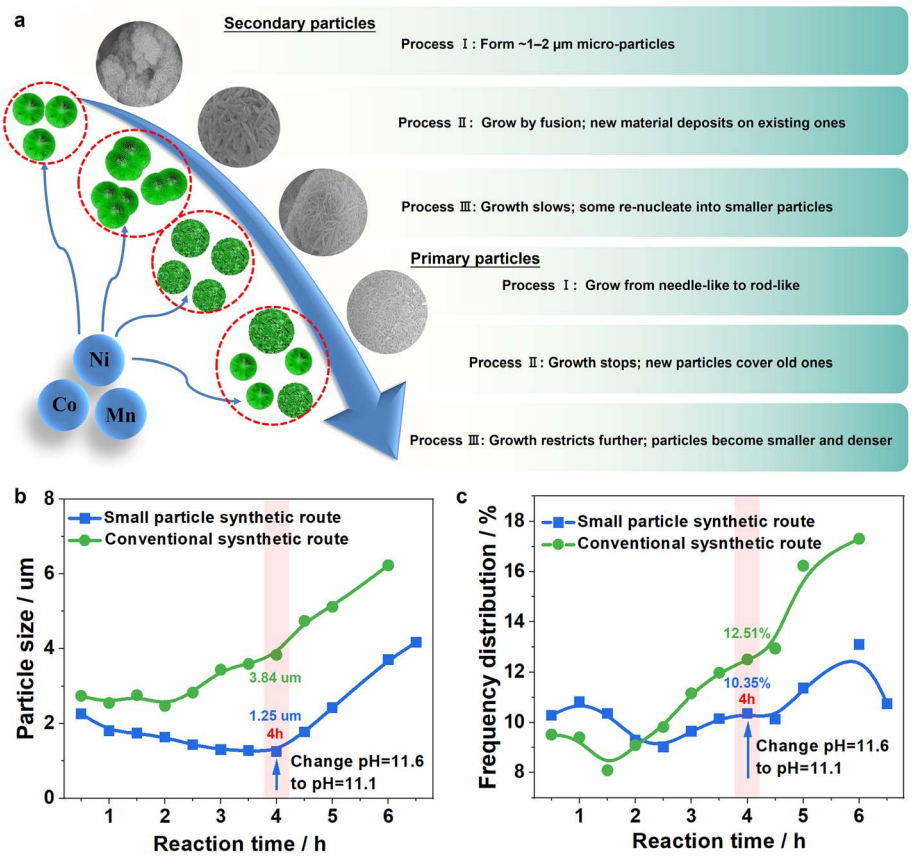


Fig. 4 (a) Growth mechanism of $Ni_{0.8}Co_{0.1}Mn_{0.1}(OH)_2$. (b) Overview of particle size evolution at different reaction times. (c) Frequency distribution analysis of $Ni_{0.8}Co_{0.1}Mn_{0.1}(OH)_2$ at various reaction times.

a narrower distribution throughout the synthesis. This highlights the superior controllability and uniformity offered by this route. Crucially, it is found that particle size evolution occurs within a critical window between two and four hours. During this stage, the precursor concentration remains high, and the secondary particles are still in their early growth phase. Thus, targeted intervention during this timeframe is most effective in adjusting the final particle characteristics. As shown in both Fig. 4b and c, adjusting the pH value from 11.6 to 11.1 at the 4-hour mark greatly affects later particle growth rates and reduces particle size broadening. This observation implies that process parameter tuning in the intermediate stage—instead of in the late stage—offers more opportunities for tailoring the morphology and microstructure of the precursors. This approach not only avoids undesired particle coarsening but also helps to generate uniformly distributed secondary particles with compact internal architectures, which are crucial for the electrochemical performance of final electrode materials.

## Conclusions

In this work, we have methodically coupled mechanistic understanding with exact synthetic control to optimize the preparation of precursors for $LiNi_{0.8}Co_{0.1}Mn_{0.1}O_2$ (NCM811) cathodes *via* a co-precipitation and solid-state sintering path. The ideal conditions for obtaining precursors with uniform spherical morphology, narrow particle size distribution, and high tap density were identified by analyzing the roles of key synthesis parameters—pH, ammonia-to-metal ratio, feed rate, and stirring speed. Additionally, an in-depth analysis of precursor evolution utilizing XRD, SEM, measurements of tap density, and particle size distribution demonstrated a three-stage growth process of secondary particles, influenced by the dynamics of precursor feed and consumption within the reactor. This mechanistic insight not only enhances our fundamental comprehension of precursor formation but also offers an innovative viewpoint on the precise regulation of microstructural evolution during the pivotal intermediate phase of scalable synthesis. This mechanism controls not only the densification and microstructural homogeneity of the final precursors but also the electrochemical behavior of the sintered NCM811. By establishing a clear structure–process–property relationship, this work emphasizes the need for precursor engineering as a basic strategy for designing high-performance cathode materials and offers a practical road map for large-scale, industrially relevant production of advanced LIB components.

## Author contributions

Hai-Yan Hu: conceptualization, visualization, data curation, writing – original draft. Yong-Chun Li: investigation, data analysis, manuscript revision. Yan-Fang Zhu: methodology, project administration. Haidong Liu: resources. Wei Xiang: supervision, resources, conceptualization. Jia-Zhao Wang: supervision, resources. Yao Xiao: supervision, funding acquisition, project administration.

## Conflicts of interest

There are no conflicts to declare.

## Data availability

The data supporting this article have been included as part of the SI.

Experimental section, crystallography data and additional figures. See DOI: **https://doi.org/10.1039/d5sc04432d**.

## Acknowledgements

This work was supported by the National Natural Science Foundation of China (52402301, 52472240, and 52202284), the Natural Science Foundation of Zhejiang Province (LQ23E020002), the Wenzhou Key Scientific and Technological Innovation Research Project (ZG2023053), the China Scholarship Council (202508330254), and the Doctoral Innovation Foundation of Wenzhou University (3162023001001). H. L. and Y. L. further acknowledge the support from the Swedish Energy Agency (P2022-00055 and P2023-00603) and ST and UP for Energy.

## References

1 R. Schmuch, R. Wagner, G. Hörpel, T. Placke and M. Winter, *Nat. Energy*, 2018, **3**, 267–278.
2 L.-Y. Kong, J.-Y. Li, H.-X. Liu, Y.-F. Zhu, J. Wang, Y. Liu, X.-Y. Zhang, H.-Y. Hu, H. Dong, Z.-C. Jian, C. Cheng, S. Chen, L. Zhang, J.-Z. Wang, S. Chou and Y. Xiao, *J. Am. Chem. Soc.*, 2024, **146**, 32317–32332.
3 Y.-C. Li, W. Xiang, Y. Xiao, Z.-G. Wu, C.-L. Xu, W. Xu, Y.-D. Xu, C. Wu, Z.-G. Yang and X.-D. Guo, *J. Power Sources*, 2019, **423**, 144–151.
4 N. Anansuksawat, T. Sangsanit, S. Prempluem, K. Homlamai, W. Tejangkura and M. Sawangphruk, *Chem. Sci.*, 2024, **15**, 2026–2036.
5 Y.-F. Liu, H.-X. Liu, Y.-F. Zhu, H.-R. Wang, J. Y. Li, Y. C. Li, H.-Y. Hu, Z.-G. Wu, X.-D. Guo and Y. Xiao, *Adv. Mater.*, 2025, **37**, e2417540.
6 G.-T. Park, N.-Y. Park, H.-H. Ryu, H.-H. Sun, J.-Y. Hwang and Y.-K. Sun, *Chem. Soc. Rev.*, 2024, **53**, 11462–11518.
7 Y.-B. Wu, H.-Y. Hu, J.-Y. Li, H.-H. Dong, Y.-F. Zhu, S.-Q. Chen, N.-N. Wang, J.-Z. Wang and Y. Xiao, *Chem. Sci.*, 2025, **16**, 3928–3937.
8 Y. Liu, T. Zeng, G. Li, T. Wan, M. Li, X. Zhang, M. Li, M. Su, A. Dou, W. Zeng, Y. Zhou, R. Guo and D. Chu, *Energy Storage Mater.*, 2022, **52**, 534–546.
9 S. Liu, J. Yang, S. Hao, S. Jiang, X. Li, O. Dolotko, F. Wu, Y. Li and Z. He, *Chem. Eng. J.*, 2024, **479**, 147607.
10 H. Liu, W. Hua, S. Kunz, M. Bianchini, H. Li, J. Peng, J. Lin, O. Dolotko, T. Bergfeldt, K. Wang, C. Kubel, P. Nagel, S. Schuppler, M. Merz, B. Ying, K. Kleiner, S. Mangold, D. Wong, V. Baran, M. Knapp, H. Ehrenberg and S. Indris, *Nat. Commun.*, 2024, **15**, 9981.

11 Z. Tan, Y. Li, C. Lei, Y. Li, X. Xi, S. Jiang, F. Wu and Z. He, *Small*, 2024, **20**, 2305618.
12 H.-Y. Hu, J.-Y. Li, Y.-F. Liu, Y.-F. Zhu, H.-W. Li, X.-B. Jia, Z.-C. Jian, H.-X. Liu, L.-Y. Kong, Z.-Q. Li, H.-H. Dong, M.-K. Zhang, L. Qiu, J.-Q. Wang, S.-Q. Chen, X.-W. Wu, X.-D. Guo and Y. Xiao, *Chem. Sci.*, 2024, **15**, 5192–5200.
13 X. Xu, H. Huo, J. Jian, L. Wang, H. Zhu, S. Xu, X. He, G. Yin, C. Du and X. Sun, *Adv. Energy Mater.*, 2019, **9**, 1803963.
14 Y. Zhang, H. Wang, Z. Li, X. Ge, K. Huang, J. Q. Huang, L. Huang, Z. Li and Y. Huang, *Adv. Energy Mater.*, 2024, **15**, 2403804.
15 S. Zhong, Y. Huang, F. Zhang, H. Wang, P. Liu, J. Liu, Z. Li, Y. Li and Z. Lu, *Adv. Funct. Mater.*, 2024, **35**, 2414602.
16 C. Feng, Y. Cao, L. Song, B. Zhao, Q. Yang, Y. Zhang, X. Wei, G. Zhou and Y. Song, *Angew. Chem., Int. Ed.*, 2025, **64**, e202418198.
17 R. Tang, J. Dong, C. Wang, A. Yin, Y. Lu, N. Li, W. Shen, J. Zhang, K. Yan, G. Zhao, B. Li, X. Wang, Y. Xu, F. Wu, Y. Su and L. Chen, *Carbon Neutralization*, 2025, **4**, e70001.
18 L. Lou, X. Liu, Y. Wang, T. Hu, Z. Wang, H. Shi, J. Xiong, S. Jing, L. Ye, Q. Guo and X. Ge, *Chin. Chem. Lett.*, 2025, **36**, 109726.
19 H.-Y. Hu, H. Wang, Y.-F. Zhu, J. Y. Li, Y. Liu, J. Wang, H.-X. Liu, X.-B. Jia, H. Li, Y. Su, Y. Gao, S. Chen, X. Wu, S.-X. Dou, S. Chou and Y. Xiao, *ACS Nano*, 2023, **17**, 15871–15882.
20 J. Y. Li, H. Y. Hu, L. F. Zhou, H. W. Li, Y. J. Lei, W. H. Lai, Y. M. Fan, Y. F. Zhu, G. Peleckis, S. Q. Chen, W. K. Pang, J. Peng, J. Z. Wang, S. X. Dou, S. L. Chou and Y. Xiao, *Adv. Funct. Mater.*, 2023, **33**, 2213215.
21 M. Zhang, L. Qiu, W. Hua, Y. Song, Y. Deng, Z. Wu, Y. Zhu, B. Zhong, S. Chou, S. Dou, Y. Xiao and X. Guo, *Adv. Mater.*, 2024, **36**, e2311814.
22 H. Zhang, X. He, Z. Chen, Y. Yang, H. Xu, L. Wang and X. He, *Adv. Energy Mater.*, 2022, **12**, 2202022.
23 D. Wang, I. Belharouak, G. M. Koenig, G. Zhou and K. Amine, *J. Mater. Chem.*, 2011, **21**, 9290.
24 H.-J. Jang, C.-H. Lee, S. Kim, S.-H. Kim and K.-B. Lee, *ACS Appl. Mater. Interfaces*, 2014, **6**, 6914–6919.
25 M. Akhilash, P. S. Salini, K. Jalaja, B. John and T. D. Mercy, *Inorg. Chem. Commun.*, 2021, **126**, 108434.
26 X. Yao, Z. Xu, Z. Yao, W. Cheng, H. Gao, Q. Zhao, J. Li and A. Zhou, *Mater. Today Commun.*, 2019, **19**, 262–270.
27 Y.-C. Li, W. Xiang, Z.-G. Wu, C.-L. Xu, Y.-D. Xu, Y. Xiao, Z.-G. Yang, C.-J. Wu, G.-P. Lv and X.-D. Guo, *Electrochim. Acta*, 2018, **291**, 84–94.
28 S. Wang, X. Zhou, T. Zhao, J. Peng, Z. Bin, W. Xing, M. Zuo, P. Zhang, W. Fan, G. Lv, W. Hua and W. Xiang, *Nano Energy*, 2024, **129**, 110008.
29 J. Yin, Z. Wu, K. Fang, Y. Zhu, K. Zhang, H. Zhang, Y. Chen, L. Li, L. Fan, K. Dong, L. Zheng, Q. Wang, H. Huang, J. Zhang, Y. Qiao and S. G. Sun, *Chem. Sci.*, 2025, **16**, 8268–8281.
30 H. Li, L. Wang, Y. Song, Z. Zhang, A. Du, Y. Tang, J. Wang and X. He, *Adv. Mater.*, 2024, **36**, e2312292.
31 W. Liang, Y. Zhao, L. Shi, Z. Wang, Y. Wang, M. Zhang and S. Yuan, *Particuology*, 2024, **86**, 67–85.
32 Y. Yang, S. Xu, M. Xie, Y. He, G. Huang and Y. Yang, *J. Alloys Compd.*, 2015, **619**, 846–853.
33 W. Liang, Y. Zhao, L. Shi, Z. Wang and S. Yuan, *Angew. Chem., Int. Ed.*, 2024, **63**, e202407477.
34 M. H. Lee, Y. J. Kang, S. T. Myung and Y. K. Sun, *Electrochim. Acta*, 2004, **50**, 939–948.
35 K. K. Cheralathan, N. Y. Kang, H. S. Park, Y. J. Lee, W. C. Choi, Y. S. Ko and Y.-K. Park, *J. Power Sources*, 2010, **195**, 1486–1494.
36 L. Qiu, M. Zhang, Y. Song, Z. Wu, Y. F. Zhu, J. Zhang, D. Wang, H. Y. Hu, H. W. Li, H. R. Liu, X. B. Jia, J. Peng, S. Chen, Z. Yang, Y. Xiao and X. Guo, *Carbon Energy*, 2022, **5**, e298.
37 W. Hua, W. Liu, M. Chen, S. Indris, Z. Zheng, X. Guo, M. Bruns, T.-H. Wu, Y. Chen, B. Zhong, S. Chou, Y.-M. Kang and H. Ehrenberg, *Electrochim. Acta*, 2017, **232**, 123–131.
38 H. Zhang, Z. Zeng, S. Cheng and J. Xie, *eScience*, 2024, **4**, 100265.
39 X. Zhou, F. Hong, S. Wang, T. Zhao, J. Peng, B. Zhang, W. Fan, W. Xing, M. Zuo, P. Zhang, Y. Zhou, G. Lv, Y. Zhong, W. Hua and W. Xiang, *eScience*, 2024, **4**, 100276.
40 Z. Wu, Y. Zhou, C. Hai, J. Zeng, Y. Sun, X. Ren, Y. Shen, X. Li and G. Zhang, *Appl. Surf. Sci.*, 2023, **619**, 156379.
41 D. Yu, G. Zeng, D. Chen, Y. Yan, Y. Zou, Q. Liu, K. Zhang, K. Fang, J. Xu, W. Yin, Y.-H. Hong, T. Qiu, H. G. Liao, X. Kuai, Y. Sun, Y. Qiao and S. G. Sun, *ACS Nano*, 2024, **18**, 27654–27664.
42 H. Zhang and J. Zhang, *eTransportation*, 2021, **7**, 100105.
43 J. Ren, H. Zhu, Y. Fang, W. Li, S. Lan, S. Wei, Z. Yin, Y. Tang, Y. Ren and Q. Liu, *Carbon Neutralization*, 2023, **2**, 339–377.
44 L. Britala, M. Marinaro and G. Kucinskis, *J. Energy Storage*, 2023, **73**, 108875.
45 M.-C. Kim, B.-C. Park, N.-Y. Park, M.-S. Kim, K.-M. Kim, J.-H. Kim, E.-J. Kim, G.-T. Park and Y.-K. Sun, *Energy Storage Mater.*, 2025, **78**, 104252.
46 Y. Koshika, H. Kaneda, S. Yoshio and Y. Furuichi, *ACS Appl. Energy Mater.*, 2022, **5**, 8169–8177.
47 W. Liang, F. Jin, Y. Zhao, L. Shi, Q. Liu, Z. Wang, Y. Wang, M. Zhang, J. Zhu and S. Yuan, *Chem. Eng. J.*, 2023, **464**, 142656.
48 X. Zhang, J. Li, T. Wang, Y. Gong and J. Zhou, *Nat. Commun.*, 2025, **16**, 5781.
49 B. Wang, X. Guo, Q. Liu, J. Dai, L. Wang, B. Luo, L. Yang, G. Du and W. Gao, *Adv. Funct. Mater.*, 2024, **35**, 2410280.
50 T. Zhang, Z. Qin, X. Long, Y. Gao, Z. Qin, N. Zhang, C. Guan and G. Chen, *Adv. Funct. Mater.*, 2025, **35**, 2500608.
51 S. Chen, P. Zhang, X. Zhou, W. Wu, X. Liu, Y. Liu, G. Feng, B. Zhang, W. Xing, M. Zuo, P. Zhang, G. Lv, Y. Xiao, S. Dou and W. Xiang, *Chem. Sci.*, 2024, **15**, 14415–14424.
52 H. Li, P. Zhou, F. Liu, H. Li, F. Cheng and J. Chen, *Chem. Sci.*, 2019, **10**, 1374–1379.
53 J. Zhang, X. Zhai, T. Zhao, X. Yang, Q. Wang, Z. Chen, M.-C. Chen, J.-J. Ma, Y.-R. Lu, S.-F. Hung and W. Hua, *J. Mater. Chem. A*, 2025, **13**, 1181–1190.

54 C. Peng, S. Liang, Y. Yu, L. Cao, C. Yang, X. Liu, K. Guo, P. Müller-Buschbaum, Y. J. Cheng and C. Wang, *Carbon Neutralization*, 2024, **3**, 1036–1091.
55 L. Qiu, M. Zhang, W. Hua, Y. Wang, Y. Deng, Z. Li, Y. Song, Z. Wu, Y. Xiao and X. Guo, *Angew. Chem., Int. Ed.*, 2024, **64**, e202417278.
56 L. Wang, J. Wang, Y. Lu, S. Fang, C. Yang, X. Wu, Y. Xiao, Y. Wang, S. Chou and S. Chen, *Chem. Soc. Rev.*, 2025, **54**, 4419–4467.
57 Z. Wang, L. Yang, C. Xu, J. Cheng, J. Zhao, Q. Huang and C. Yang, *Green Carbon*, 2023, **1**, 193–209.
58 J. Darga and A. Manthiram, *Adv. Funct. Mater.*, 2024, **34**, 2408642.
59 M. Chang, F. Cheng, W. Zhang, M. Liao, Q. Li, C. Fang and J. Han, *ACS Nano*, 2025, **19**, 712–721.
60 M. Zhang, J. Li, Q. Pang, W. Hua, Y. Deng, M. Tang, W. Pang, Z. Wu, B. Zhong, Y. Xiao, L. Qiu and X. Guo, *Adv. Energy Mater.*, 2025, **15**, 2406031.
61 Y.-C. Li, W.-M. Zhao, W. Xiang, Z.-G. Wu, Z.-G. Yang, C.-L. Xu, Y.-D. Xu, E.-H. Wang, C.-J. Wu and X.-D. Guo, *J. Alloys Compd.*, 2018, **766**, 546–555.
62 Y. Zhang, S. Hao, F. Pei, X. Xiao, C. Lu, X. Lin, Z. Li, H. Ji, Y. Shen, L. Yuan, Z. Li and Y. Huang, *Natl. Sci. Rev.*, 2024, **11**, nwae254.